



Mantle convection interacting with magma oceans

R. Agrusta, A. Morison, S. Labrosse, R. Deguen, T. Alboussière, P. J. Tackley, F. Dubuffet

► To cite this version:

R. Agrusta, A. Morison, S. Labrosse, R. Deguen, T. Alboussière, et al.. Mantle convection interacting with magma oceans. *Geophysical Journal International*, 2020, 220, pp.1878-1892. 10.1093/gji/ggz549 . insu-03710133v2

HAL Id: insu-03710133

<https://insu.hal.science/insu-03710133v2>

Submitted on 17 Mar 2023

HAL is a multi-disciplinary open access archive for the deposit and dissemination of scientific research documents, whether they are published or not. The documents may come from teaching and research institutions in France or abroad, or from public or private research centers.

L'archive ouverte pluridisciplinaire **HAL**, est destinée au dépôt et à la diffusion de documents scientifiques de niveau recherche, publiés ou non, émanant des établissements d'enseignement et de recherche français ou étrangers, des laboratoires publics ou privés.

Mantle convection interacting with magma oceans

R. Agrusta¹,¹ A. Morison,¹ S. Labrosse¹,¹ R. Deguen,¹ T. Alboussière,¹ P.J. Tackley² and F. Dubuffet¹

¹ *Université de Lyon, ENSL, UCBL, CNRS, LGL-TPE, 46 allée d'Italie, F-69364 Lyon, France. E-mail: roberto.agrusta@univ-lyon1.fr*

² *Department of Earth Sciences, Institute of Geophysics, ETH Zürich, Sonneggstrasse 5, 8092 Zürich, Switzerland*

Accepted 2019 December 2. Received 2019 December 2; in original form 2019 July 4

SUMMARY

The presence of a magma ocean may have characterized the beginning of terrestrial planets and, depending on how the solidification has proceeded, the solid mantle may have been in contact with a magma ocean at its upper boundary, its lower boundary, or both, for some period of time. At the interface where the solid is in contact with the liquid the matter can flow through by changing phase, and this affects convection in the solid during magma ocean crystallization. Linear and weakly non-linear analyses have shown that Rayleigh–Bénard flow subject to two liquid–solid phase change boundary conditions is characterized by a non-deforming translation or weakly deforming long wavelength mode at relatively low Rayleigh number. Both modes are expected to transfer heat very efficiently, at least in the range of applicability of weakly non-linear results for the deforming mode. When only one boundary is a phase change, the critical Rayleigh number is also reduced, by a factor of about 4, and the heat transfer is also greatly increased. In this study we use direct numerical simulations in 2-D Cartesian geometry to explore how the solid convection may be affected by these boundary conditions for values of the Rayleigh number extending beyond the range of validity of the weakly non-linear results, up to 10^3 times the critical value. Our results suggest that solid-state convection during magma ocean crystallization may have been characterized by a very efficient mass and heat transfer, with a heat flow and velocity at the least twice the value previously thought when only one magma ocean is present, above or below. In the situation with a magma ocean above and below, we show that the convective heat flow through the solid layer could reach values of the same order as that of the black-body radiation at the surface of the magma ocean.

Key words: Composition and structure of the mantle; Phase transitions; Mantle processes; Numerical modelling; Planetary interiors.

1 INTRODUCTION

Partial or even complete melting of the silicate mantle may have occurred early in the history of rocky planets, and depending on the phase diagram involved (e.g. Thomas *et al.* 2012; Boukaré *et al.* 2015), the solid mantle may have crystallized upwards and/or downwards leading to a solid mantle bounded above and/or below by molten layers, commonly called magma oceans (e.g. Debaille *et al.* 2007; Labrosse *et al.* 2007; Elkins-Tanton 2012; Solomatov 2015). Petrological experiments and thermodynamics calculation have shown that chemical composition controls significantly the melting curves of mantle rocks (Thomas & Asimow 2013; Boukaré *et al.* 2015; Andrault *et al.* 2017), and that the location of the first solids within the mantle depends on the slope of their melting curves compared to the isentropic temperature gradient in the magma. The solid crystallizes from the bottom if the isentropic gradient is smaller than the melting temperature gradient (e.g. Thomas & Asimow 2013) and from the top if the adiabatic gradient is larger

that the melting one (e.g. Mosenfelder *et al.* 2007). The comparison between the two slopes must be done locally, at each depth, and the curvature of the two temperature profiles matters. Fiquet *et al.* (2010) obtained a curved liquidus whereas Andrault *et al.* (2011) obtained a liquidus with a nearly constant slope, for different compositions and using slightly different experimental techniques. The curved liquidus implies that the magma ocean starts crystallizing at intermediate depth while the straight liquidus implies a crystallization from the bottom up (Thomas *et al.* 2012). Moreover, at the lowermost mantle conditions, crystallization may lead to the formation of solids lighter (Fe depleted) than the surrounding melt (Boukaré *et al.* 2015), and this would favor the formation of a basal magma ocean and eventually sustain the scenario with a solid bounded between two magma oceans (Labrosse *et al.* 2007; Boukaré *et al.* 2015). A situation with a basal ocean is also currently encountered in icy satellites like Enceladus, Europa, Titan, where the shallow icy layer is in contact with liquid water ocean and where possibly a high-pressure ice layer underlies the buried ocean (e.g. Khurana

et al. 1998; Pappalardo *et al.* 1998; Grasset *et al.* 2000; Tobie *et al.* 2003, 2006; Baland *et al.* 2014; Čadež *et al.* 2016).

Whatever the relative position of the solid compared to the ocean is, the existence of solid–liquid phase change at the boundary of a solid mantle is thought to strongly affect its dynamics (Deguen 2013; Labrosse *et al.* 2018) and this is the subject of this paper.

Usually, convection models in solid mantles assume a non-penetrating boundary condition at the horizontal boundaries of the solid shell, where the free-surface boundary condition is modeled as a free-slip boundary condition on an undeformed surface. This approximation is valid as long as the dynamic topography generated by convective stresses is small and is affected only slowly by surface processes (Ricard *et al.* 2014). This approximation has been used for mantle convection models as it operates in the current Earth and planets (Schubert *et al.* 2001), but also in the presence of a magma ocean (Ballmer *et al.* 2017; Maurice *et al.* 2017). However, at the boundary between the solid and liquid, matter may flow through by changing phase. This requires that the latent heat released in regions of freezing (inflow for the solid) is transferred efficiently to regions where it is consumed for melting (outflow). Whether this happens depends on how fast latent heat is transferred in the liquid region compared to the rate at which topography is generated by solid viscous flow (Alboussière *et al.* 2010; Deguen *et al.* 2013; Deguen 2013). Indeed, if the heat transfer in the liquid is able to erase the topography formed by viscous deformation, the lithostatic stress due to the topography variation will not balance the viscous stress of the convective solid, and the liquid–solid boundary can be considered as semi-permeable (Deguen *et al.* 2013; Deguen 2013). This process, that leads to semi-permeable boundary condition, has been shown to strongly affect the dynamics of the solid and the associated heat transfer leading for example to a translation dynamics in the Earth’s inner core in contact with the liquid outer core (Alboussière *et al.* 2010; Monnereau *et al.* 2010; Deguen *et al.* 2013; Mizzon & Monnereau 2013; Deguen *et al.* 2018), whereas only recently, attention has been paid on its effect on the evolution of the solid mantle (Deguen 2013; Labrosse *et al.* 2018; Morison *et al.* 2019).

Morison *et al.* (2019) looked at the effect of semi-permeable solid–liquid phase change boundaries on the development of the first mantle overturn, during magma ocean crystallization of the silicate mantle of the Earth, Mars and Moon. They show that solid–liquid phase change boundary conditions make the timescale of the first overturn decrease by several orders of magnitude compared to the case where solid–liquid phase change is not taken into account (Ballmer *et al.* 2017; Maurice *et al.* 2017; Boukaré *et al.* 2018). Moreover, Labrosse *et al.* (2018) performed both linear and weakly non-linear analysis to show that Rayleigh–Bénard flow in a 2-D Cartesian geometry, subject to one semi-permeable boundary, representing the simplest scenario during solid mantle formation, presents a heat transfer efficiency much higher than the classical values obtained with non-penetrating boundary conditions. Moreover, their study shows that the flow is characterized by a non-deforming translation mode or weakly deforming long-wavelength mode if the flow is allowed at both boundaries of the solid mantle. Both translation and weakly deforming modes are able to transfer heat very efficiently, and may have characterized mantle dynamics during the primordial epochs of Earth or of larger size terrestrial planets.

In this study, using 2-D Cartesian numerical simulations, we explore how solid-state Rayleigh–Bénard convection may be affected by the presence of one or two solid–liquid phase change(s) at horizontal boundary(ies). We compare the results of the present finite

amplitude calculations to the weakly non-linear results of Labrosse *et al.* (2018) and discuss the applicability of the latter to finite amplitude situations at high Rayleigh number, and the likely consequences of these boundary conditions on the primordial evolution of the Earth or other terrestrial planets.

2 METHOD

2.1 Governing equations

Solid-state mantle convection is described by the system of conservation equations for mass, momentum and energy for an incompressible fluid with infinite Prandtl number and in the Boussinesq approximation. These equations, rendered dimensionless using the thickness H of the solid mantle for length, the diffusion time H^2/κ for time, with κ the thermal diffusivity, κ/H for velocity and $\eta\kappa/H^2$ for pressure, with η the viscosity, are:

$$\nabla \cdot \mathbf{u} = 0, \quad (1)$$

$$\nabla^2 \mathbf{u} - \nabla p + \text{Ra}(T - T_c)\mathbf{z} = 0, \quad (2)$$

$$\frac{\partial T}{\partial t} + \mathbf{u} \cdot \nabla T = \nabla^2 T \quad (3)$$

with $\mathbf{u} = (v, w)$ the velocity, p the dynamic pressure, T the temperature and T_c the steady conduction solution, t the time, \mathbf{z} the unit vector in the vertical direction and Ra the Rayleigh number:

$$\text{Ra} = \frac{\alpha g \rho_s \Delta T H^3}{\kappa \eta}, \quad (4)$$

with α the thermal expansion coefficient, g the acceleration of gravity, ρ_s the density of the solid, ΔT the temperature difference between the lower and upper boundaries.

This set of equations neglects many of the complexities of mantle convection: in this first study, we assume a Newtonian rheology with a constant viscosity, we do not consider volumetric heat generation, all physical parameters are assumed uniform and constant and no compositional effect is included. Although we recognize the importance of these complexities to understand mantle dynamics (Schubert *et al.* 2001), we consider the simplest possible convective system to isolate the effects of the phase change boundary condition.

2.2 Treatment of the solid–liquid phase changes

At the boundary between a solid mantle and a liquid of the same composition, a flow through the phase change can take place, depending on how fast latent heat is transferred in the liquid region (Deguen *et al.* 2013). Stresses in the solid lead to the formation of topography of the solid–liquid interface and convective heat transfer in the liquid tends to homogenize temperature and suppress that topography. On the one hand, if the topography is able to build because the heat transfer in the liquid region is slow, the radial velocity at interface is limited by the weight of the topography (classical dynamic topography balance) and the flow across the boundary is effectively inhibited. On the other hand, when heat transfer in the liquid is fast, it can destroy the topography by transporting heat from places where crystallization occurs to places where melting happens, and the flow through the boundary is allowed. To include this process, the solid–liquid phase change is accounted for by considering the variation in the stress field and the associated dynamic pressure at the phase boundary. Details can be found in previous papers (Deguen 2013; Deguen *et al.* 2013; Labrosse *et al.* 2018)

and the derivation of the boundary condition is only shortly recalled here.

Across the solid–liquid boundary the total stress must be continuous and, if the topography slope and the viscous stress and dynamic pressure in the liquid side are assumed small and can be neglected, the vertical stress equilibrium acting along the undeformed phase boundary is

$$(\rho_s - \rho_l^\pm) g h^\pm + 2\eta \frac{\partial w}{\partial z} - p = 0. \quad (5)$$

The first term is the differential stress between the solid and liquid hydrostatic pressures, with ρ_s and ρ_l the solid and liquid density, respectively, and h the topography height, the second term and third term (p) are the viscous stress and the dynamic pressure on the solid side, w being vertical velocity. The $+$ and $-$ exponents refer to the upper and lower boundaries, respectively. Note that Chambat *et al.* (2014) argue for a discontinuity of traction across the boundary and propose to add two terms to the balance eq. (5). A preliminary analysis has shown that these two terms are negligible for applications to mantle convection and they are omitted here for simplicity.

At the solid–liquid boundary, like any phase change, the reaction is accompanied by release and absorption of latent heat, during freezing and melting, respectively. Because the interface between solid and liquid cannot accumulate or lose heat, the discontinuity of heat flow at the interface must equilibrate the release or absorption of latent heat due to the reaction. This may be expressed by the Stefan condition,

$$\rho_s L v_\phi = -q_s + q_l, \quad (6)$$

where the term on the left represents the heat production due to freezing or melting, with L the latent heat and v_ϕ the freezing (negative for melting) rate. The right-hand-side is the heat flow difference across the boundary, and the subscript s and l refer to solid and to liquid respectively. The heat flow difference of the right-hand side is dominated by convective heat transport in the liquid side, and for the sake of simplicity the right side of eq. (6) can be expressed by the advective heat flux on the liquid. Moreover, the freezing (or melting) rate (v_ϕ) can be approximated by the vertical velocity (w) across the boundary, if the topography is in quasi-steady state (i.e. if vertical advection of the boundary is balanced by melting and freezing).

Under these conditions eq. (6) leads to (see Deguen *et al.* 2013; Labrosse *et al.* 2018, for details):

$$w \equiv \frac{h^\pm}{\tau_\phi}, \quad (7)$$

τ_ϕ being the characteristic phase-change timescale for transferring latent heat from region where it is released (freezing, around topography depression) to places where it is consumed (melting, around topography highs), and is defined as:

$$\tau_\phi = \frac{\rho_s L}{\left(\rho_l c_{pl} u_l \left(\frac{dT_l}{dz} - \frac{dT_{ad}}{dz} \right) \right)^\pm}, \quad (8)$$

where c_{pl} is the heat capacity, u_l the characteristic liquid velocity and $\frac{dT_l}{dz}$ and $\frac{dT_{ad}}{dz}$ are the melting temperature Clapeyron slope and the isentropic gradient in the melting region, respectively. The explicit development of eqs (7) and (8) can be found in Deguen *et al.* (2013). Using eq. (7) and introducing the viscous timescale for building

topography,

$$\tau_\eta = \frac{\eta}{|\rho_s - \rho_l^\pm| g H}, \quad (9)$$

eq. (5) becomes, in dimensionless form:

$$\pm \Phi^\pm w + 2 \frac{\partial w}{\partial z} - p = 0, \quad (10)$$

where $\Phi = \tau_\phi / \tau_\eta$ is the phase-change number and represents the ratio between the characteristic phase-change and viscous timescales. For a large value of Φ , the phase change condition (eq. 10) implies a small value of w . This can be interpreted considering that, when $\tau_\eta \ll \tau_\phi$, the topography forms in response to stress in the solid and the solid flow is limited by the buoyancy of the topography, which makes the vertical velocity effectively drop to zero at the boundary, which leads to an effectively non-penetrating classical free-slip boundary condition. On the other hand, for the opposite situation when $\tau_\eta \gg \tau_\phi$, the topography is erased faster than it is generated. The removal of the associated buoyancy leads to a non-zero velocity across the interface and the boundary is permeable.

The continuity of the horizontal traction across the boundaries leads to the classical free-slip boundary condition,

$$\frac{\partial u}{\partial z} + \frac{\partial w}{\partial x} = 0. \quad (11)$$

Note however, that contrary to the classical calculations assuming a non-penetrating boundary condition, the second term in eq. (11) is identically zero in our model.

2.3 Numerical approach and set-up

The equation described in Sections 2.1 and 2.2 are solved using the finite-volume code StagYY (Tackley 2008). The mass and momentum eqs (1) and (2) are discretized as a unique linear system of equations inverted using a direct solver for sparse matrices (UMFPack for sequential calculations, MUMPS for parallel calculations; Amestoy *et al.* 2001, 2006), whereas the energy eq. (3) is solved in an explicit manner, using a total variation diminishing (TVD) method for the advection term.

The mechanical boundary conditions are periodic on the vertical sides, and free-slip (eq. 11) on the top and bottom domain boundaries, where eq. (10) is also applied. The thermal boundary conditions are the Dirichlet condition of fixed temperature of 0 and 1 at the top and bottom, respectively. However, resolving numerically the boundary layers on the melting front of the flow at low values of the phase change number (Φ) is difficult at large Rayleigh number. Indeed, as shown by the analytical solution for the translation mode of convection when both boundaries have a phase change, a thermal boundary layer (TBL) of thickness $1/w$ exists in the solid side (Labrosse *et al.* 2018) and since the velocity can be very large, it requires a huge number of grid points to be properly resolved. Moreover, even if extreme grid refinement can be used in the boundary layers, the stability of the explicit time-stepping scheme requires a extremely small time step which renders calculations at high Rayleigh number inaccessible. The analytical solution for the translation mode and the weakly non-linear analysis for the deforming mode (Labrosse *et al.* 2018) show however that regions where the TBL is very thin are those where flow is toward the boundary and therefore are not prone to convective instabilities. Moreover, the temperature difference in these TBLs are tiny. In that sense, these regions play little role in the global dynamics and can be modeled using the theory developed by Labrosse *et al.* (2018).

In that case, the thin TBL needs not to be resolved numerically and the Dirichlet boundary condition is replaced by an effective Robin one that depends on the vertical velocity w . The Dirichlet condition that applies at the boundary is replaced by a condition that applies on the interior side of the thin boundary layer. In practice, when the flow is toward the boundary ($w < 0$ at the bottom, $w > 0$ at the top), the vertical temperature gradient should be null, $\partial\theta/\partial z = 0$, whereas flow going away from the boundary carries the information of the boundary temperature and the Dirichlet condition is applied, $\theta = 0$, with θ the deviation of temperature with respect to the steady-state conduction profile. This condition is written as:

$$\Gamma^\pm \theta + (1 - \Gamma^\pm) \frac{\partial\theta}{\partial z} = 0, \quad (12)$$

where Γ^\pm is a smooth approximation of the Heaviside function depending on the vertical velocity:

$$\Gamma^\pm = \frac{1}{2} \left[1 + \tanh \left(\pi \frac{\mp w + \frac{w_0}{2}}{\frac{w_0}{2}} \right) \right], \quad (13)$$

with w_0 the velocity range along which Γ varies from 0 to 1, defined depending on the problem. For a large velocity toward the boundary ($w \ll -w_0/2$ at the bottom, $w \gg w_0/2$ at the top), $\Gamma \sim 0$ and we get a Neumann boundary condition, $\partial\theta/\partial z = 0$, whereas for flow away from the boundary or slow flow toward the boundary, we get the classical Dirichlet boundary condition, $\theta = 0$. Using eq. (12) the heat carried by diffusion across the thermal boundary layer is ignored and heat transport is done entirely by advection across the boundary. A similar approach has been already used to study the convection pattern with fast surface erosion or important magmatism in hot planets (Ricard *et al.* 2014). We checked that, for cases with intermediate velocity at the boundary that can be modeled using both boundary conditions, the results do not depend on the choice of boundary condition. We are therefore confident that the thermal boundary condition (12) can be used to model the phase change at high Rayleigh number.

The initial temperature conditions are described case by case in the results Section 3. The model domain has different mesh resolution depending of the problem, and it ranges from 18 to 128 gridpoints for unit length.

3 RESULTS

We performed 323 simulations in 2-D Cartesian coordinates (the full simulation list is presented in the supplementary material) to systematically investigate the convection style, the thermal structure and heat transfer efficiency in the solid mantle when it is bounded by one or two solid–liquid phase change boundaries. We investigate the effect of the phase change (Φ^\pm) and Rayleigh (Ra) numbers, which allows us to have an overview of possible convection patterns during magma ocean crystallization. In this first exploration, we do not consider the effects of many ingredients that are commonly thought to play a role in mantle convection: spherical geometry, volumetric heating, compositional variations, temperature- and depth variation of physical properties. We make this choice in order to restrict this first study to a tractable set of independent parameters and compare the results to the well studied situation of Rayleigh–Bénard convection.

3.1 Convection with a magma ocean above and below

Let us first consider the situation where both the top and bottom boundaries are the seat of a phase change between the convecting

solid and the magma oceans. This situation may have happened if the solid mantle crystallized from the middle, up- and downward (Labrosse *et al.* 2007; Thomas *et al.* 2012; Boukaré *et al.* 2015). For simplicity, we consider only the situations with an equal value of the phase change parameter at the top and bottom boundaries, which we call simply Φ for both sides.

3.1.1 Non-deforming translation mode

Labrosse *et al.* (2018) showed that a steady-state translation mode of convection can exist when both top and bottom boundaries are phase change interfaces. In that mode, a uniform purely vertical upward or downward flow in the solid is maintained by the buoyancy associated with a nearly uniform temperature, equal to that of the boundary at which the flow enters. This analytical solution is a good test of the numerical method.

To investigate the ability to develop a translation mode, we have performed numerical simulations, in a rectangular domain with aspect ratio $A = 4$, with a finite small phase-change number $\Phi = 0.01$ for both top and bottom sides. The choice of these parameters is justified by the fact that, for such a low value of Φ , the critical Rayleigh number for the onset of the translation mode is $Ra_{ct} = 24\Phi = 0.24$ and this mode is favored over a deforming mode if the aspect ratio of the domain is smaller than the critical wavelength of the deforming mode, which is approximately 115 (Labrosse *et al.* 2018). The reduced Rayleigh number $\varepsilon_t = (Ra - Ra_{ct})/Ra_{ct}$ investigated ranges from 0.01 to 100 (Table S1). The numerical results show that steady state vertical translation occurs in the solid. The dimensionless vertical velocity (w) increases with the Rayleigh number in a way that was predicted by the analytical solution for a steady-state translation (Labrosse *et al.* 2018, Fig. 1a). Fig. 1(b) shows the temperature profiles obtained by the numerical simulations compared to the temperature profile predicted by the analytical solutions. Numerical solutions nicely reproduce theoretical results, and this validates our numerical method. The temperature profile obtained at low values of the reduced Rayleigh number ($\varepsilon_t < 1$) diverges from the conductive profile by an amount proportional to the velocity (Labrosse *et al.* 2018). At high Rayleigh numbers (high translation velocity), the profile assumes a form with a constant temperature equal to the temperature at the inflow boundary (0 for downward flow and 1 for upward flow), whereas on the opposite side the temperature drops (or rises) to the boundary temperature in a thermal boundary layer of thickness $\delta \sim 1/w$ (Labrosse *et al.* 2018). Contrary to classical Rayleigh–Bénard convection where the flow is driven by horizontal density contrast, in the translation mode, the uniform topography of each boundary, $h = \tau_\phi w$, is maintained by the buoyancy associated with difference between the nearly uniform temperature and conductive profile that decreases linearly with height. Moreover, in the translation mode at high Rayleigh number, heat is mainly advected by the translation, and the difference between the top and bottom conductive heat fluxes is equal to the advective heat flux (Labrosse *et al.* 2018). This implies that, at high Rayleigh numbers ($\varepsilon_t \gg 1$), the heat flux scales linearly with the Rayleigh number, on the contrary to classical Rayleigh–Bénard convection where the heat flux scales as $Ra^{1/3}$.

3.1.2 Non-translating mode

The simulations to study the non-translating modes of convection are performed in a model domain with aspect ratio equal to the critical wavelength, $A_c = 2\pi/k_c$, with k_c the wavenumber for which

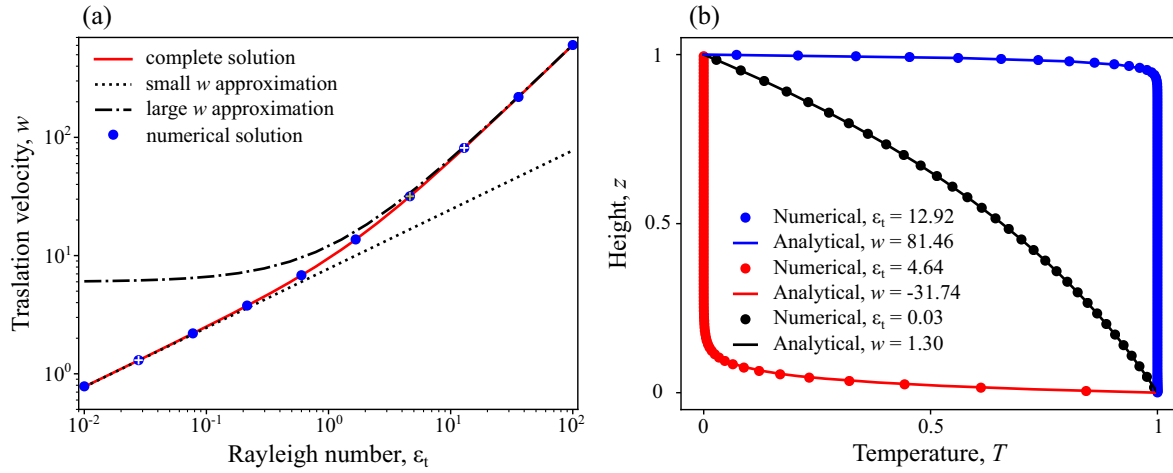


Figure 1. Non-deforming translation mode. (a) Translation velocity (w) plotted against the reduced Rayleigh numbers (ε_t), compared to the theoretical predictions (Labrosse *et al.* 2018). The blue symbols are the numerical simulations, and the white crosses indicate the simulations in (b). Solid, and dashed lines are the theoretical results. (b) Temperature profiles for relatively slow and fast velocities, both upward and downward compared with the theoretical profiles.

the critical Rayleigh number is minimum. A_c increases with the decrease of the phase-change number Φ as $\sqrt{128\pi/9\Phi}$ for small Φ and tends to the classical $2\sqrt{2}$ at large Φ (Labrosse *et al.* 2018). For this study we have investigated 5 values of Φ , ranging from 10^{-1} to 10^3 , and the aspect ratio ranges from ~ 36 to ~ 2.8 , respectively. Wider and narrower aspect ratios of respectively 1.5 and 0.5 times A_c have been used, too. We performed numerical simulations with the supercritical Rayleigh number $Ra_{sc} = \frac{Ra}{Ra_{Nt}}$ ranging from $10^{0.25}$ to 10^3 (Table S2). The critical Rayleigh number (Ra_{Nt}) refers to the critical Rayleigh number for the non-translating mode and must not be confused with the one for the translation mode [$Ra_{ct} = 12(\Phi^+ + \Phi^-)$]. In this study, we use the subscript ‘Nt’ to indicate the non-translating mode, and ‘t’ the translation one. For low values of Φ , $Ra_{Nt} \simeq Ra_{ct} - 0.3\Phi^2$, whereas for high values of Φ , Ra_{Nt} increases up to reach the critical value for a classical Rayleigh–Bénard convection $\frac{27\pi^4}{4}$ (Labrosse *et al.* 2018). The limit between low and high Φ regimes can be assumed to occur where $24\Phi = \frac{27\pi^4}{4}$, that is at $\Phi = 27.39$.

The temperature initial condition is:

$$T(x, z) = 1 - z + 0.05 \sin(\pi z) \cos(k_c x) \quad (14)$$

which represents a conductive profile with a cosine perturbation of wavenumber k_c , maximum at the centre ($z = 0.5$) and zero at the horizontal boundaries.

Fig. 2 gives an overview of the convective flows obtained by the numerical simulations for three values of Ra_{sc} and three values of Φ . At $\Phi = 0.1$, convection is mostly characterized by alternating vertical up- and downward flow, whereas at higher Φ the flow is similar to the situation with classical free-slip boundary conditions. For intermediate cases, like for $\Phi = 10$, the flow is still able to pass throughout the phase changes, but it presents a substantial horizontal component compared to the lowest phase change number cases. At high values of Φ , for example $\Phi = 1000$, the flow across the phase-change boundaries appears completely limited and the solution resembles the classical one for Rayleigh–Bénard convection with free-slip boundary conditions. This behaviour agrees with the prediction of the weakly non-linear analysis (Labrosse *et al.* 2018).

Fig. 2 shows well the effect of Φ and Ra_{sc} on the thermal structure of the solution. For $\Phi = 10^3$, we observe the classical behaviour

of Rayleigh–Bénard convection with the thickness of boundary layers and the associated up- and downwelling currents that decreases with Ra_{sc} . Conversely, the regions between up- and downwelling currents where the temperature is approximately uniform and close to 0.5, hereafter the isothermal cores, become thicker as Ra_{sc} increases. A markedly different behaviour is observed for low values of Φ ($\Phi \leq 0.1$ on the Fig. 2) for which the thickness of vertical currents does not relate to the thickness of boundary layers. In addition, the boundary between the isothermal cores and the vertical currents sharpens with the increase of the Rayleigh number, and the temperature becomes more uniform in each region. To describe the thermal structure of the convective system more quantitatively, we compute the width of the isothermal core. To define the limits of the isothermal core we use the horizontal profile of the vertically averaged temperature and the limits are defined where the temperature is the average of the mid-value and the extrema (e.g. Grigné *et al.* 2005). The isothermal core size normalized by the domain width is plotted against $\varepsilon_{Nt} = Ra_{Nt} - 1$ on Fig. 3(a). For high values of Φ ($\Phi > 100$) the width of the isothermal core increases with the Rayleigh number. This is the typical behaviour of classical (closed boundaries) Rayleigh–Bénard convection in which plume width decreases with the Rayleigh number value, like the thickness of boundary layers from which they originate, as $Ra^{-\frac{1}{3}}$. We show in Fig. 3(a), for comparison, the relationship between the isothermal core width and the Rayleigh number for the classical Rayleigh–Bénard cases, as:

$$\frac{W_{IsoCore}}{A} = 0.5 - 2.87Ra^{-\frac{1}{3}} \quad (15)$$

with $A = 2\pi/k_c$ the aspect ratio of computational domain. Eq. (15) is obtained by $W_{IsoCore} + Nu^{-1} \frac{1+\sqrt{2}}{\sqrt{2}} = 0.5A$, with $\frac{1+\sqrt{2}}{\sqrt{2}}$ the correction due to the plume lateral heat diffusion, and assuming the classical scaling law for the dimensionless heat flux (Nusselt number, Nu) as function of the Rayleigh number, valid for closed boundary conditions (Fig. 5a). The width of the isothermal core also increases with Ra at intermediate phase change number ($\Phi = 10$) but, in that case, it saturates at a value smaller than 0.5, the maximum value that can be reached for infinitely thin plumes. On the other hand, it decreases for the smaller values of Φ , leading to wider up- and downwelling currents.

For the non-translating mode solutions obtained with Φ in the low range, $\Phi < 27.39$, the maximum and minimum temperature

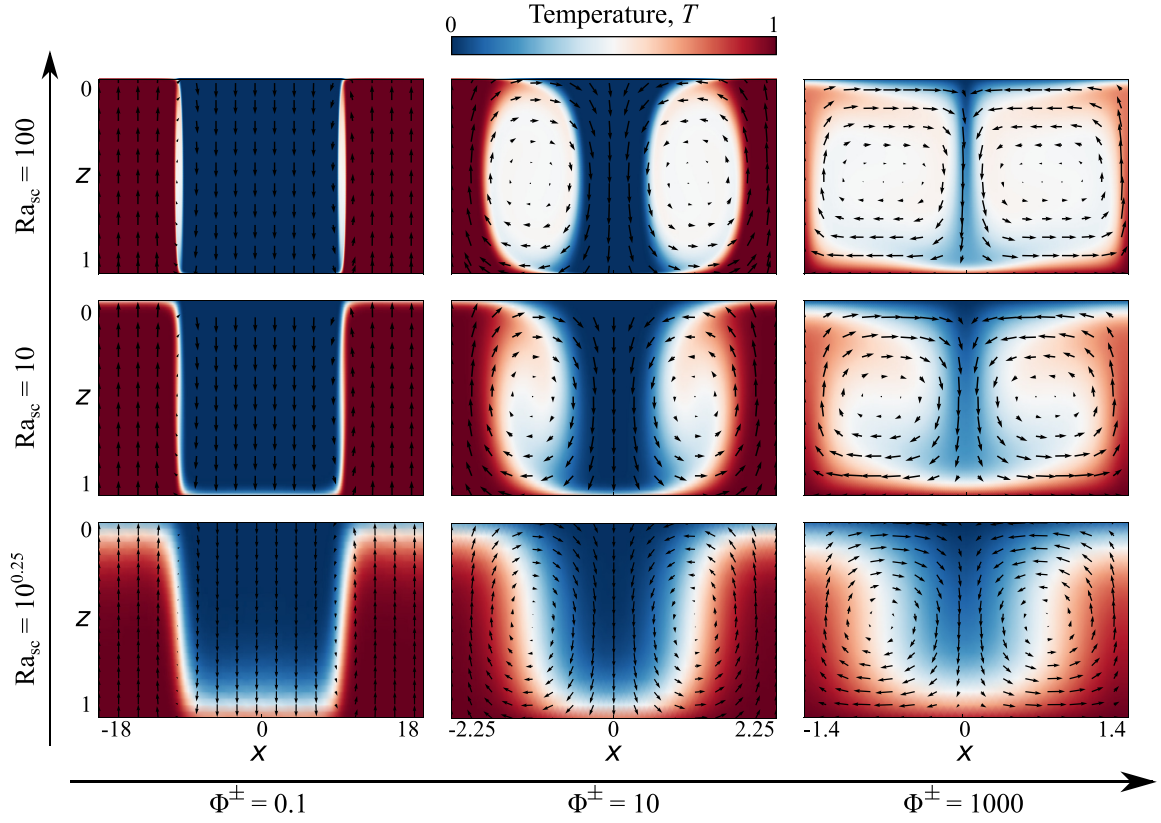


Figure 2. Convection modes with two solid–liquid change boundaries. Snapshots of temperature (colour) and velocity (arrows) for different cases investigated. The value of Φ increases from left to right, and the value of Ra_{sc} from the bottom to the top, as indicated by the axes. Note that the horizontal scale depends on the value of Φ .

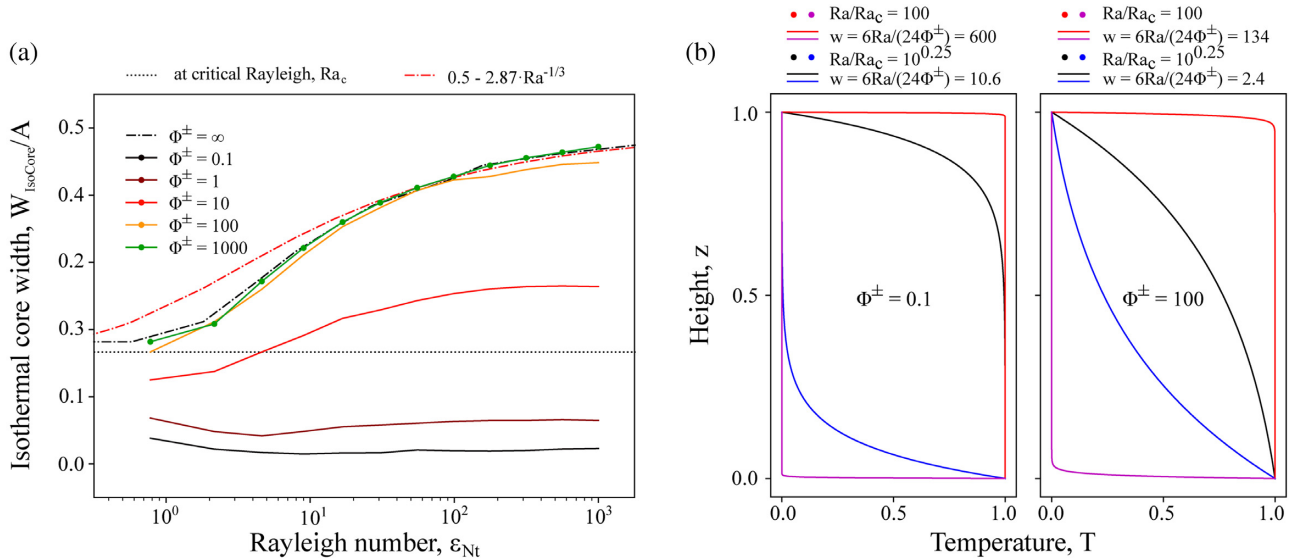


Figure 3. Thermal structure of convection with two phase change boundaries. (a) Normalized width of the isothermal core between up- and downwelling currents as function of ϵ_{Nt} (see text for details). The dash-dotted and dotted black lines represent the width obtained by the numerical results for a classical free-slip Rayleigh–Bénard problem ($\Phi^\pm = \infty$), and at the critical Rayleigh number. The red dash-dotted line is the predicted scaling for non-penetrating boundary condition. (b) Temperature as function of height in the up- and downwelling currents for cases at $\Phi = 0.1$ and $\Phi = 100$ for the Ra_{sc} as indicated in the legend. The dots represent the numerical solutions obtained from StagYY, whereas the solid lines are the profiles predicted by the theory for the pure translation solution for the same values of the Rayleigh number.

profile respectively of the cold and hot current perfectly match the profile predicted by theory for the translation mode (Fig. 3b), which therefore provides a good prediction of the solution for small Φ . The similarity between the translation and non-translation velocity at lower Φ can be explained by the low value of the phase change number, which promotes mainly vertical flow at the expenses of the horizontal one. The similarity with the translation solution disappears when Φ increases, with the transition that occurs for a value of Φ somewhere between 1 and 10. For large values of Φ , the vertical flow velocity is lower than the one predicted for the translation velocity. This agrees with colder and hotter profiles, respectively, for the up- and downwelling current compared to the profile predicted by the translation theory (Fig. 3b).

The existence of two types of solutions for the same set of parameters, one as a uniform translation and one with deformation, raises the question of their relative stability and the one that would be most likely chosen in natural situations. Labrosse *et al.* (2018) showed that slightly above the critical Rayleigh number for the translation mode, there is a region in the (k, Ra) space where the steady translation is unstable with respect to a deforming mode. The region shrinks with the decrease of Φ , meaning that the translation solution becomes more stable. In other words, for any value of Φ , there is a value of the Rayleigh number above which the translation solution is stable. On the other hand, the stability of the deforming mode of convection with respect to the translation one was not studied but the increasing stability of the translation solution when increasing the Rayleigh number suggests that the deforming mode of convection could also become unstable with respect to translation. Without exploring systematically this question, we performed calculations in the same range of parameters as presented above, Rayleigh numbers, Φ and aspect ratio A , but starting from an initial temperature condition characterized by a conductive profile with a random thermal anomaly with amplitude of 0.05 (Table S3). Starting with a random initial perturbation is closer to natural situations and is known to lead to different stable solutions, or to planforms with defects, in Rayleigh–Bénard convection. Fig. 4 shows snapshots of representative cases that we computed. We obtained solutions with a wavelength that differ from the one predicted by linear stability, or with up- and downwelling blocks of different width, like the case of $Ra_{sc} = 100$ and $\Phi = 0.1$. We also get a translation solution in some cases, when the Rayleigh number is large enough, like for $Ra_{sc} = 100$ and $\Phi = 1000$. Note that, for the models presented with $\Phi = 0.1$ in Fig. 4, despite running for a total dimensionless duration of $\Delta t = 8.5$ for $Ra = 10$ and for $\Delta t = 0.05$ for $Ra = 100$, the system has not yet reached steady state and may still evolve toward a translation solution. In particular, the case for $\Phi = 0.1$ and $Ra_{sc} = 100$ shows a clear asymmetry between up- and downwelling currents, the upwelling regions gaining with time. We expect it to ultimately run in an upward translation mode.

The heat transfer efficiency of the non-translating mode of convection is studied by computing the dimensionless heat flux and the RMS velocity (V_{rms}), for all parameter sets investigated, but ignoring the simulations that show pure translation that have been discussed above and are already well explained by the analytical theory of Labrosse *et al.* (2018). In Fig. 5 we show Nu and V_{rms} plotted against the Rayleigh number, for different values of Φ . The case with classical boundary conditions as well as the exact solution for the translation velocity and the Nusselt number predicted by weakly non-linear analysis (Labrosse *et al.* 2018) are plotted for reference, too. As expected, for $\Phi = 1000$, the solution roughly follows the scaling for classical Rayleigh–Bénard convection. On the other hand, for smaller values of Φ , both V_{rms} and Nu increase

more steeply with Ra than for non-penetrating boundary conditions. For $\Phi \leq 1$, the numerical solutions are found to closely match the prediction of the weakly non-linear analysis, for the whole range of parameters investigated, and in particular Nusselt number values in excess of 10^3 . This is somewhat unexpected since this first order development is only supposed to be valid very close to the onset of convection. This is another expression of the simplicity of the solution which exhibits alternative up- and down-ward translation regions, each very similar to the pure translation solution for which the velocity and Nusselt numbers increase linearly with Ra at large values of Ra . Indeed, for each set of solution with the same value of Φ we fit the relation $Nu = Nu_0 Ra^\alpha$, and $V_{rms} = V_0 Ra^\beta$, and the resulting scaling law are shown in the plot legends. In the Rayleigh number range investigated, the exponent α of 0.36 and β of 0.66 for the case $\Phi = 1000$ are similar to the exponents for a classical Rayleigh–Bénard convection (e.g. Jaupart & Mareschal 2011). As Φ decreases, both exponents tend to 1, showing the linear relationship of heat flux and velocity with the Rayleigh number, already proved for the pure translation solution (Labrosse *et al.* 2018). Moreover, for cases at low phase change number ($\Phi \leq 10$) the coefficient of proportionality Nu_0 , and V_0 , both scale as Φ^{-1} , as shown for the translation mode (Labrosse *et al.* 2018). The heat flux and velocity obtained by the weakly non-linear analysis represent well the results from direct numerical simulations for very small value of Φ ($\Phi \leq 1$). On the other hand, for $10 \leq \Phi \leq 100$, the heat flux and RMS velocity from numerical solutions diverge at higher Rayleigh number values from analytical predictions, which is the usual behaviour for Rayleigh–Bénard convection.

3.2 Convection with a magma ocean above or below

The situation with only one boundary having a phase change is encountered in several cases. The case with a liquid ocean below the solid layer is relevant to the surface ice-shell of some icy satellites of Jupiter and Saturn (e.g. Khurana *et al.* 1998; Pappalardo *et al.* 1998; Grasset *et al.* 2000; Tobie *et al.* 2003; Baland *et al.* 2014; Čadež *et al.* 2016) and possibly for the early Earth with a basal magma ocean (Labrosse *et al.* 2007). The case with a liquid on top of the solid may be currently relevant for high pressure ice layers below a buried ocean in the largest icy satellites (e.g. Grasset *et al.* 2000; Tobie *et al.* 2006) and for an upwardly crystallizing magma ocean in young terrestrial planets (Solomatov 2015). In the Cartesian geometry investigated in this paper, both situations are symmetrical to one another and we only study one of them, with a magma ocean below. This is done considering a finite value for the phase change number only at the bottom boundary (Φ^-), while for the top one we consider Φ^+ to be infinite, in order to impose the classical non-penetrative free-slip condition. We perform the calculations using a model domain with aspect ratio equal to the critical wavelength, $A_c = 2\pi/k_c$, and imposing the same initial temperature condition as above (eq. 14).

Before discussing all the results with only the phase change at the bottom, let us consider one case to discuss and to prove the symmetry between the situations with a magma ocean above and below. Fig. 6 shows the final snapshots of two runs with the same parameters except for the boundary conditions, one having the $\Phi^- = \infty$ and $\Phi^+ = 0.1$ and the other $\Phi^- = 0.1$ and $\Phi^+ = \infty$. Both cases were run in a box of aspect ratio 4.978 corresponding to the wavelength of the most unstable mode at the onset of convection. After a time of about 0.05 during which convection proceeded with this initial wavelength, a transition occurred to a solution with a

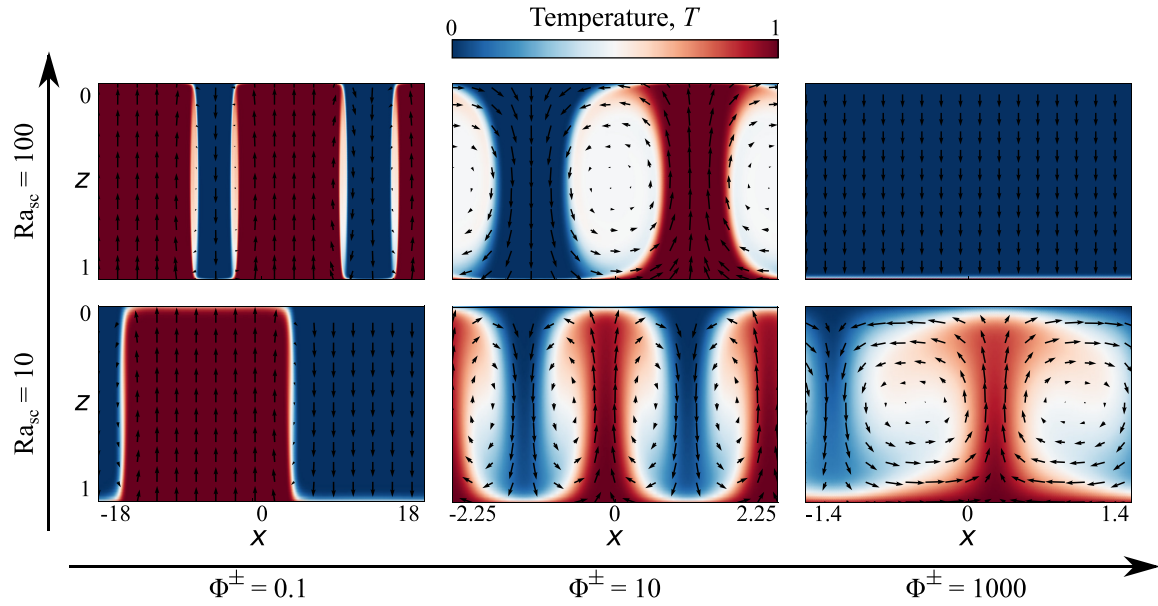


Figure 4. Convection patterns with two solid-liquid change boundaries, obtained with a random initial perturbation. Snapshots of temperature (colour) and velocity (arrows) for different cases investigated. The phase change parameter Φ increases from left to right, and the supercritical Rayleigh number Ra_{sc} from the bottom to the top, as indicated on the axes.

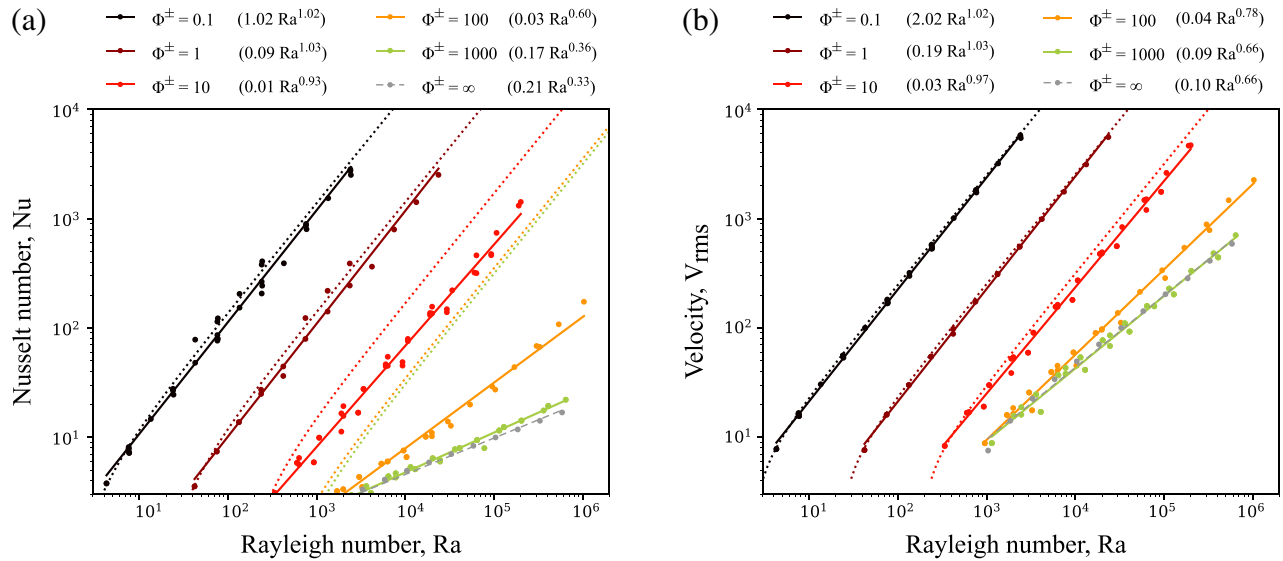


Figure 5. Heat transfer efficiency by solid-state mantle convection bounded by two magma oceans. (a) Nusselt number and (b) RMS velocity against the Rayleigh number for different values of the phase change number, as labeled. Coloured solid symbols represent results of all cases investigated. The dotted lines represent the predictions by Labrosse *et al.* (2018), using the weakly non-linear analysis for the heat flux and the exact solution of the translation mode for the velocity, whereas the gray dashed and the coloured solid lines represent the fit for each value of the phase number studied as indicated in the legend for each figures.

wavelength that is half the width of the computation domain, before resuming to a solution having the original wavelength, as displayed on the Fig. 6(a). As convection proceeds, the system alternates between solutions with one or two plumes. The two situations appear clearly symmetrical from one another: in the case of melting at the top, the flow is characterized by hot plumes with a cold diffuse return flow, whereas when the phase change is at the bottom, the flow is dominated by cold downwelling plumes and a diffuse hot return flow. The temperature in the return flow is equal to that of the boundary from which it originates with a boundary layer to match

the opposite temperature (Fig. 6b). The thickness of that boundary layer controls the heat flow in that situation and its scaling is the subject of this subsection.

For our systematic study in the case of phase change condition only at the bottom, we investigated 5 values of Φ^- , ranging from 0.1 to 1000, with a corresponding aspect ratio between 5 and 2.8, respectively. The range of supercritical Rayleigh number (Ra_{sc}) is from $10^{0.025}$ to $10^{3.25}$ (Table S4), the lower Rayleigh number cases allowing us a detailed comparison with the predictions of the weakly non-linear stability analysis (Labrosse *et al.* 2018). For the

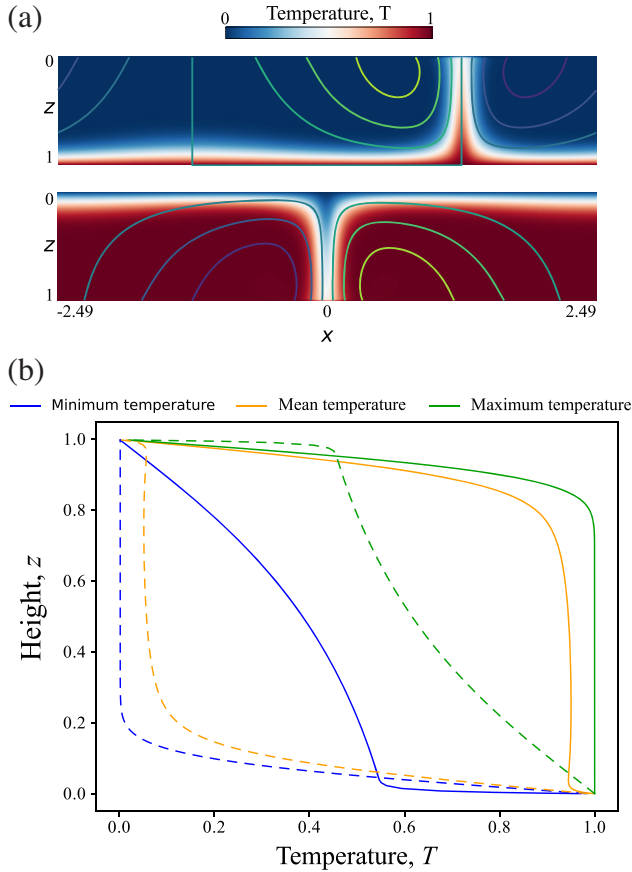


Figure 6. Solution for convection bounded by a liquid above or below. (a) Snapshots show the temperature field in colour and the streamlines at the end of the run ($t = 0.18$), with a phase change boundary condition above (top panel) or below (bottom panel), (b) The vertical profiles of minimum, mean and maximum temperature. The dashed and solid lines represent the profiles for the case with a magma ocean above and below, respectively. The Rayleigh number is $Ra = 10^4$. We used the horizontal periodicity of the solution to avoid the plume in the upper panel to be on the boundary, which it originally was.

computations at relatively high Rayleigh number ($Ra_{sc} \geq 10^{2.75}$) and $\Phi^- \leq 10$, we applied at the bottom the Robin temperature boundary condition (eq. 12), assuming a threshold velocity w_0 based on the RMS velocity for a case without phase change at similar Ra_{sc} , $w_0 = 0.5V_{rms}$. The numerical solutions for nine cases for Φ^- of 0.1, 10 and 1000 and for Ra_{sc} of $10^{0.25}$, 10 , 10^3 are shown in Fig. 7. The temperature and velocity field show that at high phase-change number ($\Phi^- = 1000$), the solution does not differ from a classical case of non-penetrating boundaries, and as Ra increases, the width of the isothermal core increases, which is the same behaviour we observed with phase change at both boundaries (Figs 2 and 3a). At lower Φ^- , a stationary cold plume, that becomes thinner as the Rayleigh number increases, characterizes the convective structure, and depending on the phase change number, at high Rayleigh number, a second cold plume can form, as shown in Fig. 7 for $\Phi^- = 0.1$ and $Ra_{sc} = 100$. The formation of a second plume occurs at $Ra_{sc} \geq 10^{0.5}$ for $\Phi^- \leq 1$ and at $Ra_{sc} \geq 10^{1.75}$ for $\Phi^- = 1$, and the convection shows periodic alternation of one and two cold plumes. In general, the gradual increase of the Rayleigh number and/or decrease of the phase change number leads to a strong increase of the mean temperature and a consequent progressive reduction of the

thickness of the top thermal boundary layer, the formation of thin and strong cold-plumes, and the disappearance of the hot thermal boundary layer at the bottom. This pattern of convection is similar to that obtained for internally heated convection (e.g. Houseman 1988; Parmentier *et al.* 1994; Sotin & Labrosse 1999), even though no volume heating is included in the present calculations.

Let us now study how the Nusselt number (Nu) and the average temperature ($\langle T \rangle$) vary at low Rayleigh numbers ($Ra_{sc} \leq 10^{0.25}$). Fig. 8 shows Nu and $\langle T \rangle$ plotted against the Rayleigh number, for different values of Φ^- , together with the prediction of the weakly non-linear analysis (Labrosse *et al.* 2018). The weakly non-linear analysis is found to provide good predictions only close to the critical Rayleigh number, as expected, the range of validity being somewhat larger for the average temperature than for the Nusselt number. For large values of Φ^- , the average temperature is close to 0.5, like for classical Rayleigh–Bénard convection, while at low Φ^- it increases more steeply as the Rayleigh number increases. The fact that the average temperature is larger than 0.5 is again similar to the situation encountered for internally heated convection.

The Nusselt number (Nu), the RMS velocity (V_{rms}) and the average temperature ($\langle T \rangle$) at higher Rayleigh numbers are plotted on Fig. 9. The Nu and V_{rms} variations are bounded between the low value of the classical Rayleigh–Bénard convection with non-penetrative conditions and the high value for low phase change number ($\Phi^- = 0.1$). The scaling law for the Nu , RMS velocity and temperature are, for $\Phi^- = 0.1$:

$$Nu = 0.37Ra^{0.33}, \quad (16)$$

$$V_{rms} = 0.2Ra^{0.66}, \quad (17)$$

$$\langle T \rangle = 1.0 - 2.64Ra^{-0.33}. \quad (18)$$

We obtained the same scaling laws for Nu and $\langle T \rangle$ as that obtained by Ricard *et al.* (2014) for mantle convection subject to fast erosion or magmatism at its surface. This indicates that different physical processes can lead to a similar physics. Moreover, as shown on Fig. 9, the pre-factors in the scaling laws for the Nusselt number and the RMS velocity (eqs 16 and 17) are about twice their counterpart for the case with non-penetrating boundary conditions, indicating a much larger heat and mass transfer when a phase change is permitted at the boundary. As suggested by Labrosse *et al.* (2018), because there is not limit to vertical flow at the bottom, the Rayleigh number is equivalent to four times the Rayleigh number of the classical not-permeable case. The ratio between the pre-factors is similar to what would be expected from this simple heuristic. Results for $\Phi^- \geq 10$ are close to that for non-penetrative boundary conditions, at least at low values of the Rayleigh number. Increasing its value makes the heat flow at the bottom increase which makes the mean temperature increase further eventually leading to a transition to a fully open bottom boundary. This transition appears to take place at $10^4 < Ra < 10^5$ for $\Phi^- = 10$, and likely at higher Ra for $\Phi^- \geq 100$. We suspect that, for large enough Rayleigh numbers, all scaling laws collapse to the one obtained in the small Φ^- limit, the results obtained here for intermediate values of Φ^- ($\Phi^- = 10, 100$) being transitional.

4 DISCUSSION

In this study, we have investigated the dynamics of a solid mantle bounded between two magma oceans or in contact with one at the

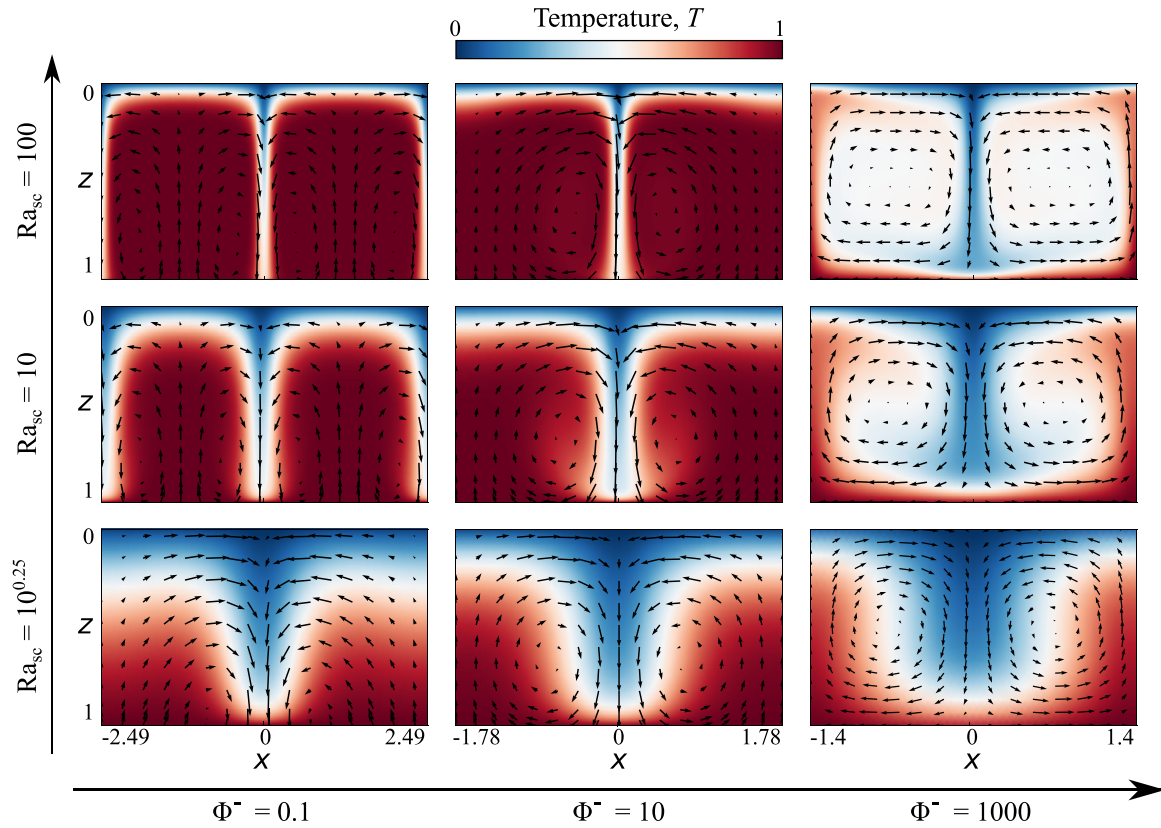


Figure 7. Convection patterns obtained with a phase change only at the bottom boundary. Snapshots of temperature (colour) and velocity (arrows) for different case investigated. Φ^- increases from left to right, and Ra_{sc} from the bottom to the top, as indicated by the axes. Note that the horizontal scale depends on the value of Φ^- .

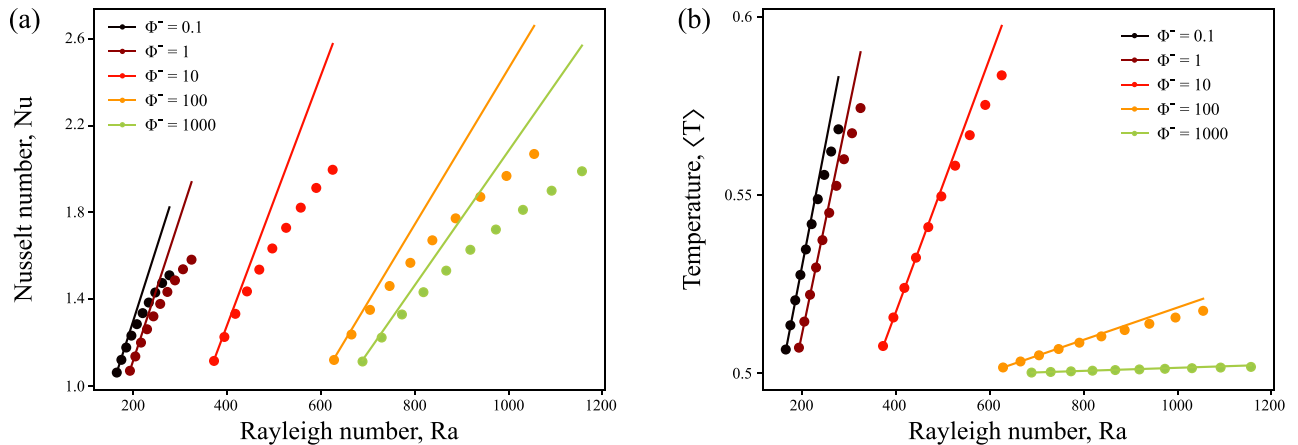


Figure 8. Heat flux and average temperature for a Rayleigh number close to the critical value for convection bounded by only one phase change boundary. (a) Nusselt number and (b) average temperature against the Rayleigh number. The lines represent the predictions of the weakly non-linear analysis.

bottom. The mantle is modeled as a 2-D layer of infinite Prandtl number fluid and the solid–liquid phase change at either or both boundaries is taken into account by imposing a boundary condition allowing a flow through the boundary. This boundary condition is controlled by a phase change parameter, Φ , which allows the system to go from easy flow-through at low Φ values to classical non-penetration at large Φ .

In many ways, the setup we used is too simplistic to be directly applied to planetary mantles but the effects of the phase change boundary condition are so drastic that it calls for a systematic study

on these effects on the simplest situation before including some of the complexities of mantle convection. Let us discuss here a few of these complexities, that may be required to include in future models, depending on the planetary object of applications, the Earth or icy satellites. The first obvious limitation concerns the chosen geometry, Cartesian instead of a spherical shell. Running models in a spherical shell is possible using StagYY (Tackley 2008) but it is quite costly in three dimensions. Using the spherical annulus geometry (Hernlund & Tackley 2008) is readily possible and is the target of a future study. Compared to the situation investigated in

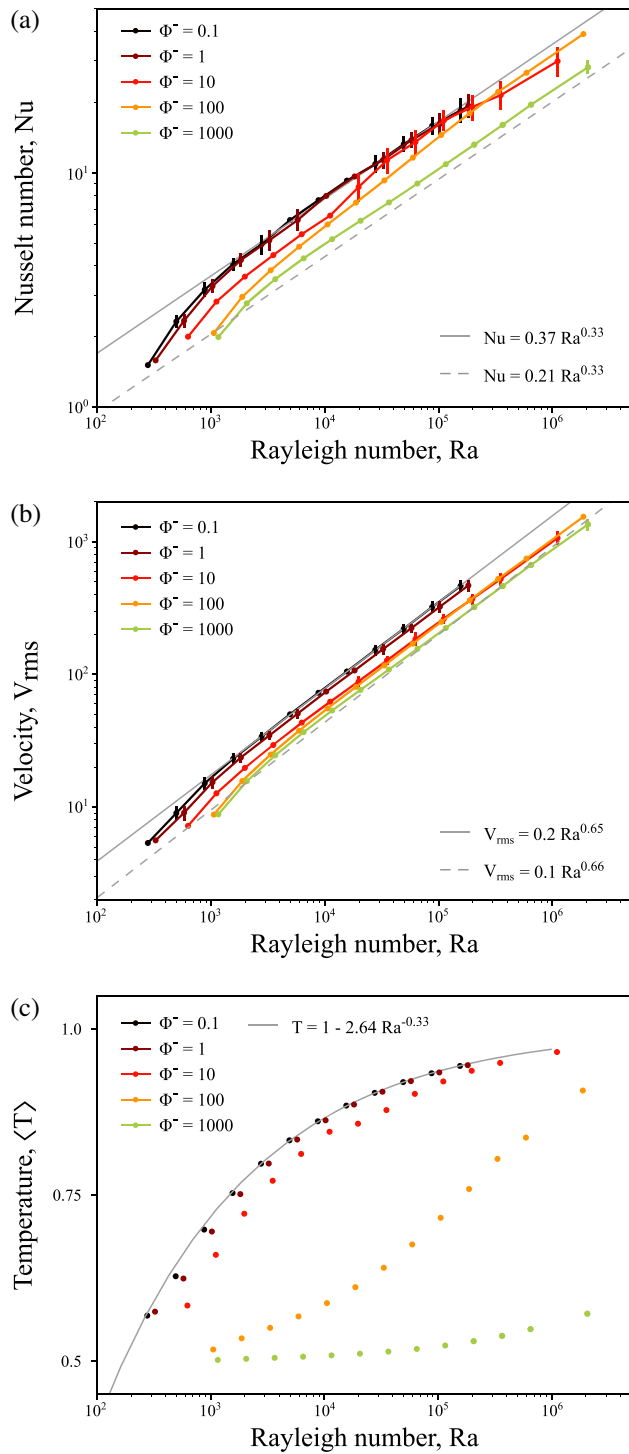


Figure 9. Heat and mass transfer characteristics for mantle convection with a solid-liquid phase change at the bottom. (a) Nusselt number, (b) RMS velocity and (c) average temperature, against the Rayleigh number. The gray solid line represents the fit for the simulation for $\Phi^- = 0.1$, and the grey dashed line the classical non-penetrative free-slip case as already shown on Fig. 5.

this paper in which the horizontal scale of the flow can tend to infinity when the phase change numbers of both boundaries are decreased, up to the uniform translation mode, the spherical shell geometry imposes a maximum wavelength that corresponds to the spherical harmonics degree 1. This mode is indeed found to be preferred when both boundaries have a low value of Φ (Deguen 2013; Morison *et al.* 2019), which corresponds to a spherical translation mode. Opposite to the situation of the translation mode in Cartesian velocity, a translation in spherical geometry is characterized by a zero horizontal average of the vertical velocity. Even if this mode of convection is predicted by the linear stability analysis, its form at finite amplitude remains to be studied. In the case with only a basal magma ocean, the dynamics is controlled by the top boundary layer, as in internally heated convection, and we expect a similar behaviour in spherical shell geometry. The main difference between the two geometries is that the situations with a magma ocean on top is not strictly symmetrical to the one with a magma ocean below in spherical geometry, although the behaviours of each situation can be qualitatively predicted from the other. Pursuing with geometrical effects, the dynamics that is modeled here should also be accompanied with the net motion of the boundaries as the magma oceans freeze or, possibly, the solid mantle remelts. The importance of this aspect depends on the velocity of the boundary motion relative to the flow velocity in the solid. During the crystallization of a top magma ocean, both velocities may be comparable and the net freezing has been included in the study of Morison *et al.* (2019) about the onset of convection. In the case of a basal magma ocean only, the net motion of the interface is expected to be slow and separation of timescales should apply. Nevertheless, the net motion of the interfaces is important, particularly when dealing with the long term evolution of the mantle. This is also associated with the evolution of the composition of magma oceans and the solid that crystallizes from it. These effects have been included in the numerical model and are the subject of our current studies. Another simplification of the present model is that we consider all physical properties uniform whereas most vary with pressure and temperature in planetary mantles. Among these, the most important one is undoubtedly the viscosity. In the case of a magma ocean above and below, the whole solid is close to the melting temperature and we do not expect its variations to affect the solutions too much, in particular since the solutions in that case have a very large wavelength with little deformation. The situation with only a basal magma ocean is quite different since the surface boundary is the one at the lowest temperature and therefore the highest viscosity but is also the one which provides the buoyancy source for the flow. Taking into account the temperature-dependence of the viscosity, we expect to obtain the same regimes as with classical boundary conditions: the small viscosity contrasts regime, the transitional regime and the stagnant-lid regime (Moresi & Solomatov 1995). The regime boundaries should however be displaced compared to the classical case, as is the value of the Rayleigh number for the onset of convection. The significance of this effect remains to be investigated. By far, the most important limitation of the present results comes from neglecting variations of composition and their effect on the melting temperature and the implied two-phase flow dynamics. First of all, as we assume incompressibility in the framework of the Boussinesq approximation, temperature gradients should in fact be interpreted as superisentropic temperature gradients, or gradient of the potential temperature. In this context, a curved liquidus as obtained by (Fiquet *et al.* 2010) that allows crystallization to start in the mid-mantle

(Mosenfelder *et al.* 2009; Boukaré *et al.* 2015), could in fact lead to a decrease of melting temperature with depth in the deep mantle. Considering first the situation where crystallization indeed starts in the mid-mantle, the upward crystallization proceeds much faster than the downward one, owing to the rapid heat transfer to the atmosphere, and we expect a temperature profile in the solid following the liquidus (Morison *et al.* 2019). As soon as the convective instability sets in, the matter at the bottom of the solid layer, which is at the highest temperature, should remelt on its way up. Treating properly this problem requires including two-phase flow dynamics, as done by Boukaré & Ricard (2017), and goes beyond the current paper. We expect however that taking into account remelting of hot solid as it moves up should enhance heat transfer even more than what is obtained in the present results, which should then be considered as conservative. The situation with only a basal magma ocean is less problematic. The existence of a basal magma ocean requires the isentropic gradient to be steeper than the melting temperature gradient. This has been proposed for the magma (Mosenfelder *et al.* 2009; Boukaré *et al.* 2015) and it is also possible for the solid. Of course, we expect that an upwelling current getting close to the upper boundary may eventually cross the solidus, leading to partial melting and volcanism as it is happening in the current mantle. This process is likely to be more pervasive with a basal magma ocean since the whole mantle, except for focused downwelling currents, is then predicted to have a potential temperature similar to that of the lower boundary. Some effort has been conducted in the recent years to account for volcanism and plutonism in large scale mantle convection models (e.g. Agrusta *et al.* 2015; Lourenço *et al.* 2018) and we expect that similar processes can coexist with a basal magma ocean. Again, the present result not taking these effects into account should be considered as conservative in terms of heat flow. The model presented in this paper neglect the effects of variations of composition even though Labrosse *et al.* (2007) proposed that fractional crystallization at the base of the mantle could lead to formation of dense piles at the bottom of the mantle. This behaviour is in fact expected to develop late in the history of the mantle, when enough of the basal magma ocean has already crystallized. The present results should apply early in the history, when the variations of composition are too small to significantly affect mantle dynamics. They may also apply to the ice layers of icy satellites in which very little salt is expected to enter. Having laid down the most important limitations that we can identify, we can still use the scaling laws obtained for the Nusselt number as function of the Rayleigh number to evaluate the heat flux and to quantify the impact that a permeable solid–liquid change boundary might have had on the thermal evolution of both bottom magma ocean and core, and on the surface magma ocean. Combining the definition of Nusselt number, Rayleigh number, and their scaling relationship $Nu = \gamma Ra^\beta$, the heat flux Q can be evaluated by the following equation:

$$Q = \gamma \left(\frac{\alpha g \rho_s}{\kappa \eta} \right)^\beta k H_s^{3\beta-1} (T_{\text{bottom}} - T_{\text{top}})^{\beta+1}, \quad (19)$$

with $k = \rho_s C_p \kappa$ the thermal conductivity, γ and β the fitting coefficients and that depend on the phase change number Φ and the problem considered. Their values are given in the Fig. 5(a) for the case with 2 magma oceans and in the eq. (16) for the case of a solid in contact with only one magma ocean. T_{bottom} and T_{top} are the bottom and top potential temperature, respectively. Obviously, the super-isentropic temperature difference depends on the thickness of the solid mantle and we follow a very simple scenario similar to that of Morison *et al.* (2019), assuming that the top and bottom boundaries are at the liquidus temperature. We assume that crystallization

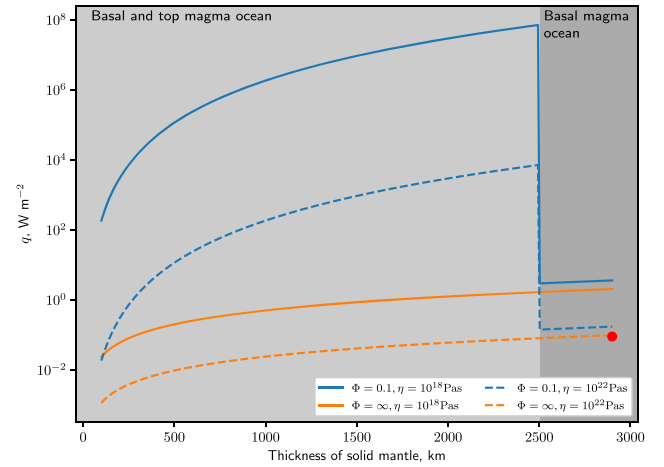


Figure 10. Heat flux density predicted as a function of the thickness of crystallized mantle. For a thickness lower than 2500 km, we assume the existence of magma oceans above and below. For a thicker solid mantle, we assume only a basal magma ocean. The blue curves are computed using the scaling law obtained for $\Phi = 0.1$, the orange ones are computed with the scaling law obtained without the effect of the phase change boundary condition. Solid and dashed curves are for different values of the solid mantle viscosity, as labeled. The red dot represents the present-day value of the mean surface heat flux.

starts at a depth of 2500 km, first upward with both magma oceans then downwards with only a basal magma ocean. For any thickness of the crystallized mantle we can compute the predicted heat flow from eq. (19) for different values of the Φ parameters. Although simplistic, this scenario allows us to compare a conservative estimate of heat transfer by solid-state convection in the early mantle to that at present and draw some implications.

For simplicity, we consider all physical parameters constant and in particular the liquidus temperature gradient, $\partial_r T_L \simeq -0.93 \text{ K km}^{-1}$ (Andrault *et al.* 2011), the isentropic temperature gradient, $\partial_r T_{AD} \simeq -0.17 \text{ K km}^{-1}$ (Katsura *et al.* 2004), which allow us to relate the super-isentropic difference to the thickness of the layer as $\Delta T \equiv T_{\text{bottom}} - T_{\text{top}} = 0.76 H_s$ with H_s in km and ΔT in K. For the other parameters, we use $g = 9.8 \text{ m s}^{-2}$, $\alpha = 2 \times 10^{-5} \text{ K}^{-1}$, $\kappa = 10^{-6} \text{ m}^2 \text{ s}^{-1}$, $\rho_s = 4 \times 10^3 \text{ kg m}^{-3}$, $C_p = 10^3 \text{ J kg}^{-1} \text{ K}^{-1}$ and, for the viscosity, either $\eta = 10^{18} \text{ Pa s}$, possibly representative of the situation where the solid is close to the solidus, or $\eta = 10^{22} \text{ Pa s}$, similar to the present-time mantle viscosity.

Fig. 10 shows the results of this simple calculation. The choice of parameters makes the heat flux density for a completely solid mantle, using the classical boundary conditions and the large viscosity, $q = 98 \text{ mW m}^{-2}$, similar to the present-day value, $q = 90 \text{ mW m}^{-2}$ (Jaupart *et al.* 2015), represented as a red dot on the figure. Decreasing the viscosity obviously leads to a larger heat flux. Having a basal magma ocean makes the heat flux 76 per cent larger, with $\gamma = 0.37$ instead of $\gamma = 0.21$ as pre-factor in the scaling relation (19). The most spectacular result is obtained with magma oceans above and below. As a comparison, a magma ocean with a surface temperature of $T_s = 3000 \text{ K}$ not surrounded by an atmosphere radiates $q = 4.6 \text{ MW m}^{-2}$ into free space. This value is obtained for a convecting solid mantle of 1200 km thickness. Including an early atmosphere on top of the magma ocean makes its surface heat flow decrease significantly (e.g. Lebrun *et al.* 2013; Hamano *et al.* 2013; Salvador *et al.* 2017) so that the value just quoted is in fact a maximum achievable surface heat flux. On the other hand, the value $\Phi = 0.1$

used to compute the results shown on Fig. 10 is likely to be overestimated, possibly by orders of magnitude. It appears therefore that if both magma oceans existed at some point in the early times, convection in the solid mantle is not a limiting factor for the cooling of the deep Earth. The reason for the ease of heat transport in that case lies in the peculiar mode of convection that develops with no or very little deformation, the viscosity playing therefore no role in the process.

5 CONCLUSIONS

In this study we have investigated the dynamics of a solid mantle bounded between two magma oceans or in contact with one at the bottom, with a semi-permeable phase-change at the solid–liquid boundary(ies). We explored systematically the parameter space to compare with and extend the results of the weakly non-linear analysis of Labrosse *et al.* (2018). For the case when the solid is bounded above and below by magma oceans, we recover the two modes of convection predicted by Labrosse *et al.* (2018): a steady-state up- or downward non-deforming translation and a deforming mode. Extending the previous results from Labrosse *et al.* (2018) to high values of the Rayleigh number shows that the solution at small values of Φ takes the form of alternating up- and downward translating blocks separated by thin deformation bands (isothermal core width ~ 1). The two vertically moving blocks have a vertical velocity and a thermal structure that closely resemble the exact analytical solution for the pure translation mode (Labrosse *et al.* 2018). Both convection modes are characterized by a very efficient heat transfer, in which the Nusselt number scales linearly with the Rayleigh number, whereas in the classical situation of Rayleigh–Bénard convection with non-penetrating boundary conditions, it scales as $Ra^{1/3}$. Consequently, we find that the predictions from the weakly non-linear analysis predict very well the behaviour of the solution for the whole range of calculations performed in this study, with a Nusselt number as high as 3×10^3 .

The situation with a magma ocean above and below the solid mantle may have occurred early in the history of Earth-or-larger-sized rocky Planets (Labrosse *et al.* 2007; Thomas *et al.* 2012; Boukaré *et al.* 2015). Assuming efficient mixing of the magma ocean, we expect the value of Φ to be less than 0.01. Applying the present results to that situation suggests that heat and mass transfer would rapidly grow to values that are orders of magnitude larger than any rate encountered in the solid mantle after full crystallization of magma oceans, of the same order or even larger than the black body heat flow at the surface of a bare magma ocean. This would promote a heat flow from the deep interior to the surface magma ocean so large that the basal magma ocean and the core would cool faster than previously thought, fast enough to drive an early dynamo.

A magma ocean that simply cools by radiating heat into space would solidify completely in a few thousand years (Monteux *et al.* 2016). Considering the effect of a dense atmosphere can elongate this period to about 10 Myr at Earth position (e.g. Abe 1997; Hamano *et al.* 2013; Lebrun *et al.* 2013; Salvador *et al.* 2017). Longer timescales can be reached for planets closer to their star (e.g. Hamano *et al.* 2013; Salvador *et al.* 2017). It is however difficult to explain with these models the apparent longevity of the Martian magma ocean, of order 100 My according to Debaille *et al.* (2007). Our result suggest that the possibility of phase change between the crystallizing mantle and the magma ocean allows for a very efficient heat transfer by convection in the solid. This means that the contribution of the heat flow from the deepest part of the

planet to the magma ocean thermal budget may not be as negligible as usually assumed. If the mantle crystallizes upward from the bottom and is in contact with only one magma ocean, the heat flux scaling obtained here would suggest a heat flow a factor of two larger than that obtained for classical non-penetrating conditions, for the same Rayleigh number. The importance of that heat flow depends then crucially on the values of poorly constrained parameters such as the viscosity of the solid mantle. On the other hand, it is quite possible that a basal magma ocean formed on Mars owing to the density inversion between olivine and silicate melt at about 8 GPa (e.g. Ohtani 1983; Agee & Walker 1993, 1988). In that case, the heat flow across the solid mantle could be orders of magnitude larger, of the same order as the radiative surface heat flux, and contribute significantly to keep the surface magma ocean liquid, as long as the basal magma ocean has not crystallized. This could help making the magma ocean on Mars last ~ 100 Myr (Debaille *et al.* 2007). Heat is not the only player in this scenario since fractional crystallization would also lead to transfer of FeO between the top and basal magma oceans changing their freezing temperature (Andrault *et al.* 2017). A full model including FeO exchange is therefore necessary to test whether this scenario could make the surface magma ocean live longer.

Considering now the case of only one magma ocean, the situation applies for the present time on icy satellites and possibly for a part of the history of the Earth (Labrosse *et al.* 2007). We only studied here the situation with a magma ocean below the solid mantle but the case with a magma ocean above is its symmetrical in the Cartesian geometry considered here (fig. 6). The results presented above show that the form of convection and the thermal structure are dramatically modified and heat and mass transfer are greatly enhanced when phase melting and freezing occurs at one boundary, even though these effects are not as drastic as in the case of two phase change boundaries. In the case of a basal magma ocean that has been investigated thoroughly here, the dynamics and thermal structure bears many similarities with internally heated convection, with narrow cold plumes descending from the upper boundary and broad high temperature return flow elsewhere. Even though volumetric heating is not included in these calculation, the bottom boundary layer is completely suppressed and no hot plume can develop. This suggests that the dynamics of the surface ice shells of icy satellites and possibly of the early Earth mantle are entirely dominated by downwelling currents, leaving no role to hot plumes. In the case of the Earth mantle, the situation is certainly more complex with fractional crystallization at the bottom possibly leading to compositional stratification, a situation that deserves further study.

In terms of heat transfer, we find that the dimensionless heat flux, the Nusselt number, scales with the Rayleigh number with an exponent equal to $1/3$, which is the same as for classical non-penetrating conditions, but with a pre-factor about 76 percent higher. This means that, for the same Rayleigh number, the thermal evolution with a basal magma ocean should be about twice faster than without it, and this imply that thermal evolution models, involving a basal magma ocean, should take that effect into account. The parametrization of the heat flow at the bottom of the solid mantle cannot rely on the existence of a boundary layer, as was assumed by Labrosse *et al.* (2007), since heat transfer happens by advection through the boundary. We expect however that, as compositionally dense material fractionally crystallizing at the bottom starts to accumulate (Labrosse *et al.* 2007), the dynamics of the bottom of the solid mantle strongly departs from the one shown here.

ACKNOWLEDGEMENTS

We would like to thank the editor Gael Choblet and two anonymous reviewers for their constructive reviews. This research has been funded by the French Agence Nationale de la Recherche under the grant number ANR-15-CE31-0018-01, MaCoMaOc.

REFERENCES

- Abe, Y., 1997. Thermal and chemical evolution of the terrestrial magma ocean, *Phys. Earth planet. Inter.*, **100**, 27–39.
- Agee, C.B. & Walker, D., 1988. Mass balance and phase density constraints on early differentiation of chondritic mantle, *Earth Planet. sci. Lett.*, **90**(2), 144–156.
- Agee, C.B. & Walker, D., 1993. Olivine flotation in mantle melt, *Earth Planet. sci. Lett.*, **114**(2–3), 315–324.
- Agrusta, R., Tommasi, A., Arcay, D., Gonzalez, A. & Gerya, T., 2015. How partial melting affects small-scale convection in a plume-fed sublithospheric layer beneath fast-moving plates, *Geochem. Geophys. Geosyst.*, **16**(11), 3924–3945.
- Alboussière, T., Deguen, R. & Melzani, M., 2010. Melting-induced stratification above the Earth's inner core due to convective translation, *Nature*, **466**, 744.
- Amestoy, P., Duff, I., L'Excellent, J. & Koster, J., 2001. A fully asynchronous multifrontal solver using distributed dynamic scheduling, *SIAM J. Matrix Anal. Appl.*, **23**(1), 15–41.
- Amestoy, P.R., Guermouche, A., L'Excellent, J.-Y. & Pralet, S., 2006. Hybrid scheduling for the parallel solution of linear systems, *Parallel Comput.*, **32**(2), 136–156.
- Andrault, D., Bolfan-Casanova, N., Nigro, G.L., Bouhifd, M.A., Garbarino, G. & Mezouar, M., 2011. Solidus and liquidus profiles of chondritic mantle: Implication for melting of the Earth across its history, *Earth planet. Sci. Lett.*, **304**, 251–259.
- Andrault, D. *et al.*, 2017. Toward a coherent model for the melting behaviour of the deep earth's mantle, *Phys. Earth planet. Inter.*, **265**, 67–81.
- Baland, R.-M., Tobie, G., Lefèvre, A. & Van Hoolst, T., 2014. Titan's internal structure inferred from its gravity field, shape, and rotation state, *Icarus*, **237**, 29–41.
- Ballmer, M.D., Lourenço, D.L., Hirose, K., Caracas, R. & Nomura, R., 2017. Reconciling magma-ocean crystallization models with the present-day structure of the Earth's mantle, *Geochem. Geophys. Geosyst.*, **18**(7), 2785–2806.
- Boukaré, C.-E. & Ricard, Y., 2017. Modeling phase separation and phase change for magma ocean solidification dynamics, *Geochem. Geophys. Geosyst.*, **18**(9), 3385–3404.
- Boukaré, C.-E., Ricard, Y. & Fiquet, G., 2015. Thermodynamics of the MgO-FeO-SiO₂ system up to 140 GPa: application to the crystallization of Earth's magma ocean, *J. geophys. Res.*, **120**(9), 6085–6101.
- Boukaré, C.-E., Parmentier, E. & Parman, S., 2018. Timing of mantle overturn during magma ocean solidification, *Earth planet. Sci. Lett.*, **491**, 216–225.
- Čadež, O. *et al.*, 2016. Enceladus's internal ocean and ice shell constrained from Cassini gravity, shape, and libration data, *Geophys. Res. Lett.*, **43**(11), 5653–5660.
- Chambat, F., Benzoni-Gavage, S. & Ricard, Y., 2014. Jump conditions and dynamic surface tension at permeable interfaces such as the inner core boundary, *C. R. Geosci.*, **346**(5–6), 110–118.
- Debaille, V., Brandon, A.D., Yin, Q.Z. & Jacobsen, B., 2007. Coupled ¹⁴²Nd–¹⁴³Nd evidence for a protracted magma ocean in mars, *Nature*, **450**, 525.
- Deguen, R., 2013. Thermal convection in a spherical shell with melting/freezing at either or both of its boundaries, *J. Earth Sci.*, **24**, 669–682.
- Deguen, R., Alboussière, T. & Cardin, P., 2013. Thermal convection in Earth's inner core with phase change at its boundary, *Geophys. J. Int.*, **194**(3), 1310–1334.
- Deguen, R., Alboussière, T. & Labrosse, S., 2018. Double-diffusive translation of Earth's inner core, *Geophys. J. Int.*, **214**(1), 88–107.
- Elkins-Tanton, L.T., 2012. Magma oceans in the inner solar system, *Ann. Rev. Earth Planet. sci.*, **40**(1), 113–139.
- Fiquet, G., Auzende, A.L., Siebert, J., Corgne, A., Bureau, H., Ozawa, H. & Garbarino, G., 2010. Melting of peridotite to 140 gigapascals, *Science*, **329**(5998), 1516–1518.
- Grasset, O., Sotin, C. & Deschamps, F., 2000. On the internal structure and dynamics of Titan, *Planet. Space Sci.*, **48**(7), 617–636.
- Grigné, C., Labrosse, S. & Tackley, P.J., 2005. Convective heat transfer as a function of wavelength: Implications for the cooling of the Earth, *J. geophys. Res.*, **110**(B3), B03409.
- Hamano, K., Abe, Y. & Genda, H., 2013. Emergence of two types of terrestrial planet on solidification of magma ocean, *Nature*, **497**, 607.
- Hernlund, J.W. & Tackley, P.J., 2008. Modeling mantle convection in the spherical annulus, *Phys. Earth Planet. Inter.*, **171**, 48–54.
- Houseman, G., 1988. The dependence of convection planform on mode of heating, *Nature*, **332**(6162), 346–349.
- Jaupart, C. & Mareschal, J.-C., 2011. *Heat Generation and Transport in the Earth*, Cambridge Univ. Press.
- Jaupart, C., Labrosse, S., Lucazeau, F. & Mareschal, J.-C., 2015. 7.06 - temperatures, heat, and energy in the mantle of the earth, in *Treatise on Geophysics*, 2nd edn, pp. 223–270, ed. Schubert, G., Elsevier.
- Katsura, T. *et al.*, 2004. Olivine-Wadsleyite transition in the system (Mg,Fe)SiO₄, *J. geophys. Res.*, **109**, B02209.
- Khurana, K.K., Kivelson, M.G., Stevenson, D.J., Schubert, G., Russell, C.T., Walker, R.J. & Polanskey, C., 1998. Induced magnetic fields as evidence for subsurface oceans in Europa and Callisto, *Nature*, **395**, 777.
- Labrosse, S., Hernlund, J.W. & Coltice, N., 2007. A crystallizing dense magma ocean at the base of the Earth's mantle, *Nature*, **450**, 866.
- Labrosse, S., Morison, A., Deguen, R. & Alboussière, T., 2018. Rayleigh-Bénard convection in a creeping solid with melting and freezing at either or both its horizontal boundaries, *J. Fluid Mech.*, **846**, 5–36.
- Lebrun, T., Massol, H., Chassefière, E., Davaille, A., Marcq, E., Sarda, P., Leblanc, F. & Brandeis, G., 2013. Thermal evolution of an early magma ocean in interaction with the atmosphere, *J. geophys. Res.*, **118**(6), 1155–1176.
- Lourenço, D.L., Rozel, A.B., Gerya, T. & Tackley, P.J., 2018. Efficient cooling of rocky planets by intrusive magmatism, *Nat. Geosci.*, **11**(5), 322–327.
- Maurice, M., Tosi, N., Samuel, H., Plesa, A.-C., Hüttig, C. & Breuer, D., 2017. Onset of solid-state mantle convection and mixing during magma ocean solidification, *J. geophys. Res.*, **122**(3), 577–598.
- Mizzon, H. & Monnereau, M., 2013. Implication of the lopsided growth for the viscosity of Earth's inner core, *Earth planet. Sci. Lett.*, **361**, 391–401.
- Monnereau, M., Calvet, M., Margerin, L. & Souriau, A., 2010. Lopsided growth of Earth's inner core, *Science*, **328**(5981), 1014–1017.
- Monteux, J., Andrault, D. & Samuel, H., 2016. On the cooling of a deep terrestrial magma ocean, *Earth planet. Sci. Lett.*, **448**, 140–149.
- Moresi, L. & Solomatov, V.S., 1995. Numerical investigation of 2d convection with extremely large viscosity variations, *Phys. Fluids*, **7**(9), 2154–2162.
- Morison, A., Labrosse, S., Deguen, R. & Alboussière, T., 2019. Timescale of overturn in a magma ocean cumulate, *Earth planet. Sci. Lett.*, **516**, 25–36.
- Mosenfelder, J.L., Asimow, P.D. & Ahrens, T.J., 2007. Thermodynamic properties of Mg₂SiO₄ liquid at ultra-high pressures from shock measurements to 200 GPa on forsterite and wadsleyite, *J. geophys. Res.*, **112**(B6), doi:10.1029/2006JB004364.
- Mosenfelder, J.L., Asimow, P.D., Frost, D.J., Rubie, D.C. & Ahrens, T.J., 2009. The MgSiO₃ system at high pressure: Thermodynamic properties of perovskite, postperovskite, and melt from global inversion of shock and static compression data, *J. geophys. Res.*, **114**(1), 1–16.
- Ohtani, E., 1983. Melting temperature distribution and fractionation in the lower mantle, *Phys. Earth planet. Inter.*, **33**(1), 12–25.
- Pappalardo, R.T. *et al.*, 1998. Geological evidence for solid-state convection in Europa's ice shell, *Nature*, **391**, 365–368.
- Parmentier, E.M., Sotin, C. & Travis, B.J., 1994. Turbulent 3-D thermal convection in an infinite Prandtl number, volumetrically heated fluid: implications for mantle dynamics, *Geophys. J. Int.*, **116**(2), 241–251.

- Ricard, Y., Labrosse, S. & Dubuffet, F., 2014. Lifting the cover of the cauldron: Convection in hot planets, *Geochem. Geophys. Geosyst.*, **15**(12), 4617–4630.
- Salvador, A., Massol, H., Davaille, A., Marcq, E., Sarda, P. & Chassefière, E., 2017. The relative influence of H₂O and CO₂ on the primitive surface conditions and evolution of rocky planets, *J. geophys. Res.*, **122**(7), 1458–1486.
- Schubert, G., Turcotte, D.L. & Olson, P., 2001. *Mantle Convection in the Earth and Planets*, Cambridge Univ. Press.
- Solomatov, V., 2015. 9.04 - magma oceans and primordial mantle differentiation, in *Treatise on Geophysics*, 2nd edn, pp. 81–104, ed. Schubert, G., Elsevier.
- Sotin, C. & Labrosse, S., 1999. Three-dimensional thermal convection in an iso-viscous, infinite Prandtl number fluid heated from within and from below: applications to the transfer of heat through planetary mantles, *Phys. Earth planet. Inter.*, **112**(3–4), 171–190.
- Tackley, P.J., 2008. Modelling compressible mantle convection with large viscosity contrasts in a three-dimensional spherical shell using the yin-yang grid, *Phys. Earth planet. Inter.*, **171**(1–4), 7–18.
- Thomas, C.W. & Asimow, P.D., 2013. Direct shock compression experiments on premolten forsterite and progress toward a consistent high-pressure equation of state for CaO-MgO-Al₂O₃-SiO₂-FeO liquids, *J. geophys. Res.*, **118**(11), 5738–5752.
- Thomas, C.W., Liu, Q., Agee, C.B., Asimow, P.D. & Lange, R.A., 2012. Multi-technique equation of state for Fe₂SiO₄ melt and the density of Fe-bearing silicate melts from 0 to 161 GPa, *J. geophys. Res.*, **117**(B10), doi:10.1029/2012JB009403.
- Tobie, G., Choblet, G. & Sotin, C., 2003. Tidally heated convection: constraints on Europa's ice shell thickness, *J. geophys. Res.*, **108**(E11), doi:10.1029/2003JE002099.
- Tobie, G., Lunine, J.I. & Sotin, C., 2006. Episodic outgassing as the origin of atmospheric methane on Titan, *Nature*, **440**(7080), 61–64.

SUPPORTING INFORMATION

Supplementary data are available at [GJI](#) online.

Table S1. List of simulations of the translation mode obtained with a phase-change number (Φ) of 0.01 for both horizontal boundaries and aspect ratio (A) of 4.

Table S2. List of simulations for the non-translating mode cases performed with the initial temperature condition of a conductive profile with a cosine perturbation (eq. 12).

Table S3. List of simulations for the non-translating mode cases obtained with a random initial temperature perturbation.

Table S4. List of simulations for the cases performed with only the phase change at the bottom boundary.

Please note: Oxford University Press is not responsible for the content or functionality of any supporting materials supplied by the authors. Any queries (other than missing material) should be directed to the corresponding author for the paper.